A human monoclonal antibody targeting a conserved pocket in the SARS-CoV-2 receptor-binding domain core

Juliette Fedry[1=], Daniel L. Hurdiss[1,2=], Chunyan Wang[2=], Wentao Li[2=], Gonzalo Obal[3], Ieva Drulyte[4], Stuart C. Howes[1], Frank J.M. van Kuppeveld[2], Friedrich Förster[1#] and Berend-Jan Bosch[2#]

[1]Cryo-Electron Microscopy, Bijvoet Centre for Biomolecular Research, Department of Chemistry, Faculty of Science, Utrecht University, Padualaan 8, 3584 CH Utrecht, The Netherlands

[2]Virology Section, Infectious Diseases and Immunology Division, Department of Biomolecular Health Sciences, Faculty of Veterinary Medicine, Utrecht University, 3584CL Utrecht, The Netherlands.

[3]Crystal and Structural Chemistry, Bijvoet Centre for Biomolecular Research, Department of Chemistry, Faculty of Science, Utrecht University, Padualaan 8, 3584 CH Utrecht, The Netherlands

[4]Materials and Structural Analysis, Thermo Fisher Scientific, Eindhoven, 5651 GG, The Netherlands.

= Contributed equally to this work.

Address correspondence to Friedrich Förster (f.g.forster@uu.nl) and Berend-Jan Bosch (b.j.bosch@uu.nl).

Abstract

SARS-CoV-2 has caused a global outbreak of severe respiratory disease (COVID-19), leading to an unprecedented public health crisis. To date, there has been over 33 million diagnosed infections, and over one million deaths. No vaccine or targeted therapeutics are currently available. We previously identified a human monoclonal antibody, 47D11, capable of cross-neutralising SARS-CoV-2 and the related 2002/2003 SARS-CoV. Here we present the structural basis of its neutralization mechanism. We describe cryo-EM structures of trimeric SARS-CoV and SARS-CoV-2 spike ectodomains in complex with the 47D11 Fab. These data reveal that 47D11 binds specifically to the closed conformation of the receptor binding domain, distal to the ACE2 binding site. The CDRL3 stabilises the N343 glycan in an upright conformation, exposing a conserved and mutationally constrained hydrophobic pocket, into which the CDRH3 loop inserts two aromatic residues. Interestingly, 47D11 preferentially selects for the partially open conformation of the SARS-CoV-2 spike, suggesting that it could be used effectively in combination with other antibodies that target the exposed receptor-binding motif. Taken together, these results expose a cryptic site of vulnerability on the SARS-CoV-2 RBD and provide a structural roadmap for the development of 47D11 as a prophylactic or post-exposure therapy for COVID-19.

Introduction

The severe acute respiratory syndrome coronavirus 2 (SARS-CoV-2) emerged from a zoonotic event in China, late 2019(*1*). To date, the resulting coronavirus induced disease 19 (COVID-19) pandemic has been responsible for over 33 million infections and over a million deaths, as of September 29, 2020(https://covid19.who.int/). SARS-CoV-2 and SARS-CoV, another highly lethal respiratory pathogen which emerged in 2002/2003(*2*), belong to the *Sarbecovirus* subgenus (genus *Betacoronavirus*, family *Coronaviridae*)(*3*). At present, no targeted therapeutics have been approved for COVID-19, meaning there is an urgent clinical need for potent antiviral therapies to halt the spread of SARS-CoV-2 and to pre-empt future outbreaks caused by SARS-like viruses. Antibodies are a promising class of drugs for combatting infectious diseases and have shown therapeutic efficacy for a number of viruses(*4*, *5*), including in the treatment of SARS and COVID-19(*6*, *7*). Such antibodies function by targeting vulnerable sites on viral surface proteins.

The coronavirus trimeric spike (S) glycoprotein, located on the viral envelope, is the key mediator of viral entry into host cells. The spike protein consists of two main parts: S1 is involved in receptor binding and S2 is the membrane fusion domain. The S1 domain itself is further subdivided into an N-terminal domain (NTD, or S1A) and a receptor binding domain (RBD, or S1B)(*8*, *9*). The spike proteins of SARS-CoV-2 (SARS2-S; 1273 residues, strain Wuhan-Hu-1) and SARS-CoV (SARS-S, 1255 residues, strain Urbani) exhibit 77.5% identity in their primary amino acid sequence and are structurally conserved. The spike trimer exists in equilibrium between a closed conformation, where all three RBD are lying flat, and a partially open conformation, where one RBD stands upright and is exposed for receptor engagement(*10-12*). Both viruses use the human angiotensin converting enzyme 2 (ACE2) protein as a host receptor, with binding mediated through interactions with the receptor-binding motif (RBM) located on the RBD, and the N-terminal helix of ACE2(*13*). The spike-mediated fusion of viral and cellular membranes is tightly regulated and triggered by a cascade of preceding events. The first step involves the attachment of SARS-CoV-2 to the target cell surface via the interaction between spike and ACE2(*13*, *14*). In the second step, the spike protein needs to be primed for membrane fusion by host proteases (e.g. cellular transmembrane serine protease 2）which cleave the spike at multiple sites(*15*), enabling shedding of S1. Finally, the free S2 catalyses the fusion of the viral and the host membranes(*16*, *17*), causing the release of the viral genome into the host cell cytoplasm.

The S glycoprotein is the primary target for neutralising antibodies, making it the main target for vaccine development(*18*). Indeed, a number of SARS-CoV-2 neutralising antibodies have

now been described(*19-33*). However, comparatively few cross-neutralising antibodies have been reported(*20*, *25*, *30*, *34*), of which only a handful have been structurally characterised(*29*, *35-37*). The most commonly identified antibodies neutralize coronaviruses by binding to the receptor interaction site in S1, blocking receptor interactions and/or promoting premature conformational change of spike to the post-fusion state. However, a smaller number of antibodies have been reported to bind sites which are distal to the ACE2 binding site. Such antibodies target the RBD-core(*27*, *35*, *37*, *38*), or even the NTD(*39*). Several promising vaccines are currently being developed but it is estimated that at least a year will be needed before they can be introduced on the market. Hence there is an urgent need for characterized antibodies to form cocktails for the treatment by passive immunization of COVID-19 patients. Combined structural and functional studies are thus required to determine the epitopes and investigate the molecular mechanisms of SARS-CoV-2 neutralizing antibodies. Moreover, such studies may identify cryptic sites of vulnerability which can guide vaccine and antiviral development(*40*).

We recently reported the first human monoclonal antibody, 47D11, capable of cross-neutralising SARS-CoV and SARS-CoV-2 at 1.3 and 3.8 nM, respectively, but its mode of engagement with the spike protein remained unclear. We thus employed structural and functional studies to decipher the molecular basis for 47D11-mediated neutralisation.

Results

47D11 specifically binds to the closed receptor binding domain

To understand how 47D11 binds to the SARS-CoV and SARS-CoV-2 spike proteins, we used cryo-electron microscopy (cryo-EM) to determine structures of prefusion stabilised ectodomain trimers in complex with the 47D11 Fab fragment. The resulting cryo-EM maps have global resolutions of 3.8 Å and 4.0 Å resolution for SARS-S and SARS2-S, respectively (Supplementary Figure1A-F). For previously reported apo S trimers, both the open and closed conformation are observed, with the latter being predominant (56% for SARS and 67% for SARS2(*11*, *41*)). Upon incubation with 47D11, only the closed conformation of the SARS spike was observed, with stochiometric binding of 47D11 to each RBD (Figure 1A). Interestingly, for SARS-CoV-2, only the partially open conformation of spike was observed, with one Fab bound to each of the closed RBDs, and the remaining open RBD unoccupied and, in principle, accessible to ACE2 binding (Figure 1B). The sub stochiometric binding observed for SARS2-S may partially explain our previous observations that 47D11 binds to the SARS-S with higher affinity than SARS2-S (equilibrium dissociation constant [K_D] of 0.745 nM and 10.8 nM, respectively)(*42*). To understand why 47D11 favours different spike conformations for SARS-CoV and SARS-CoV-2, we first superposed the Fab-bound structures with their apo

113 counterparts. Compared to the apo partially open SARS2-S structure, the RBDs are less
114 compact when 47D11 is bound (Figure 2A). The apo conformation of the closed RBD would
115 preclude binding of 47D11 through steric hindrance. To accommodate the bound Fab, this
116 RBD shifts outwards by ~7 Å (Figure 2B). Unlike S309 and H014(*35*, *38*), two other RBD-core
117 targeting SARS neutralizing antibodies, there was no indication from our cryo-EM data that
118 47D11 can bind to the open conformation of the SARS2-S RBD. In line with this,
119 superimposition of open and closed SARS2-S RBDs revealed that 47D11 would clash with
120 the adjacent N-terminal domain (NTD) and the N331 glycan in the latter conformation (Figure
121 2C). Similar to SARS2-S, the RBDs of the 47D11 bound SARS-S are also less compact than
122 the reported apo fully closed structure (Figure 2D). However, in contrast to SARS2-S, there is
123 a potential stabilising salt bridge between D463, located on the receptor binding ridge (RBR),
124 and R18 on the 47D11 light chain (Figure 2E). Indeed, the RBR exhibits the most prominent
125 structural differences between SARS2-S and SARS-S(*13*). This epitope distal loop, located
126 within the ACE2-binding region, contains an essential disulfide bridge in both viruses, but is
127 more compact in SARS-S. In order to test whether the epitope distal RBR impacts binding of
128 47D11 to the SARS-S and SARS2-S, we swapped loop residues 470-490 (SARS2-S
129 numbering) and produced chimeric ectodomains. In support of our hypothesis, the SARS2-S,
130 containing the SARS-S RBR loop, exhibited increased binding to 47D11. However, we did not
131 observe an equivalent loss of binding for the chimeric SARS-S, suggesting that other
132 differences in protein sequence or quaternary structure may be involved (Figure 2F). Taken
133 together, our data shows that 47D11 binding to the closed RBDs of the trimeric spike protein
134 has differing outcomes for SARS-S and SARS2-S, trapping them in the fully closed and the
135 partially open conformation, respectively (Figure S2).
136
137 **47D11 targets a conserved hydrophobic pocket in the RBD**
138 The 47D11 epitope is distinct from the ACE2 binding site (Figure 3A), consistent with our
139 recently reported functional data(*42*). The protein/glycan epitope is located on the core domain
140 of the SARS-S and SARS2-S RBD. As expected, the mode of binding is highly similar for
141 SARS-S and SARS2-S (Figure S3A), with the aligned 47D11:RBD complexes having an
142 RMSD value of 1.4 Å. The paratope is composed of CDRL3 and CDRH3 loops, that form a
143 primarily hydrophobic interaction with the RBD surface of ~830 $Å^2$ and ~800 $Å^2$ for SARS-S
144 and SARS2-S, respectively. The side chain of 47D11 CDRL3 tryptophan W94 stacks against
145 the N330/N343 (SARS/SARS2) glycan tree, contributing to its stabilization in an upright
146 conformation (Figure 3B). This reveals a hydrophobic pocket into which the CDRH3 loop
147 projects, allowing Fab residues W102 and F103 to interact with RBD core residues F338,
148 F342, Y365, V367, L368, F374 and W436 (F325, F329, Y352, V354, L355, F361 and W423
149 in SARS-S) – figure 3B and S3B. Interestingly, this pocket is normally shielded by the N343

150 glycan in previously reported SARS2-S structures (Figure 3C-D)(*11*, *12*). In order to
151 accommodate the CDRH3 loop residues, the helix encompassing residues 365-370 is
152 displaced outwards by 2 Å, creating 55 $Å^3$ of solvent accessible volume which is not present
153 in the apo RBD (Figure 3C-D and Figure S3C-D). Of note, the region directly below this
154 hydrophobic pocket was recently shown bind to linoleic acid, which stabilises the closed
155 conformation of spike by spanning two adjacent RBDs(*43*). However, the distance between
156 the 47D11-bound RBDs is too great to be bridged by linoleic acid. Consistent with this, no
157 density consistent with linoleic acid was present in any of our reconstructions.
158
159 To verify the 47D11 epitope, we introduced alanine mutations at each of the identified contact
160 residues in the context of full-length spike protein. In addition, a spike mutant with the naturally
161 occurring V367F minority variant was generated(*44*). Binding of 47D11 to surface expressed
162 wildtype and mutant spike proteins was assessed by flow cytometry. Soluble Fc-tagged ACE2
163 and the RBD core binding mAb CR3022 were taken along as controls. The V367F substitution
164 and the alanine substitute at this position only had a minor effect on 47D11 antibody binding
165 (Figure 3E), consistent with data showing that this polymorphism had no effect on
166 neutralisation of SARS2-S pseudo type virus (Figure 3I). Collectively, this indicates that 47D11
167 would be effective against this SARS-CoV-2 variant. In contrast, all other amino acid
168 substitutions in the hydrophobic core not only reduced cell-surface binding by 47D11 (Figure
169 3E), but also prevented binding of ACE2 and the core targeting antibody CR3022, despite
170 being distal to their respective interaction sites (Figure 3F-G and Figure S4A-B). Total cellular
171 expression of mutants was comparable to wildtype spike protein as demonstrated by an
172 antibody targeting the C-terminal appended Flag-tag on the spike proteins (Figure 3H),
173 suggesting that mutations in the RBD hydrophobic core have a detrimental effect on protein
174 folding, compromising the tertiary structure of the RBD. A recent study reported deep
175 mutational scanning of SARS2-S RBD residues, revealing how mutation of each of the RBD
176 residues affects expression of folded protein and its affinity for ACE2(*45*). When the mean
177 mutation effect on expression was mapped on the 47D11 bound RBD, we observed that the
178 hydrophobic pocket, targeted by 47D11, is highly mutationally constrained (Figure 3J).
179 Another SARS-CoV and SARS-CoV-2 neutralising antibody, S309, targets a similar region to
180 47D11, but here the orientation of the N343 glycan prohibits access to the hydrophobic pocket,
181 similarly to apo structures (Figure 3K)(*35*). The 47D11 epitope is distinct from other reported
182 RBD-core targeting antibodies/nanobodies, such as CR3022, H014 and VHH-72 (Figure
183 S4)(*27*, *38*, *46*).
184
185 Comparative sequence analysis revealed that the 47D11 epitope is highly conserved across
186 circulating SARS-like viruses (Figure 4A and S5). This is in contrast to the ACE2 binding

region which exhibits the greatest sequence variability. In order to assess whether 47D11 has broad reactivity, we recombinantly expressed the RBD from WIV16, HKU3-3 and HKU9-3 and analysed 47D11 binding to these related sarbecoviruses. The results demonstrated that 47D11 can bind to the WIV16 RBD with similar affinity to SARS-S and SARS2-S (Figure 4B). Closer inspections of the aligned RBD amino acid sequences revealed that the N343 glycosylation site, as well as the hydrophobic pocket, are strictly conserved between these three SARS-like viruses (Figure 4C). Therefore, the lack of binding observed for HKU3-3 and HKU9-3 may be due to epitope adjacent sequence differences which preclude binding of the CDRH3 loop. Nevertheless, the potent binding observed for WIV16 underscores the potential of 47D11 as a treatment for future outbreaks caused by SARS-like viruses.

In conclusion, our structural and functional analyses demonstrate that 47D11 is able to unmask a conserved and mutationally constrained epitope on the SARS-CoV-2 RBD by stabilising the N343 glycan in an upright conformation. Once this site is exposed, the CDRH3 loop is able to insert two aromatic residues into the hydrophobic core of the RBD, inducing conformational changes which lead to the formation of a 55 $Å^3$ cavity. This cryptic site offers an attractive target for design of vaccines and targeted therapeutics, such as small molecule inhibitors. The 47D11 epitope is distal to the ACE2 receptor binding motif, rationalising its ability to cross-neutralize SARS-CoV and SARS-CoV-2 independently of receptor-binding inhibition. Our structural analysis also shows that 47D11 exhibits differing conformational selectivity for the SARS-S and SARS2-S, providing a possible explanation for the differences in observed binding affinity. Given that 47D11 selects for the partially open conformation of the SARS-CoV-2 spike protein, we speculate that 47D11 may render the spike more susceptible to other monoclonal antibodies which target the exposed receptor-binding subdomain, making it a prime candidate for combination treatment. Antibody combinations targeting non-overlapping epitopes may act synergistically permitting a lower dosage and an increased barrier to immune escape(*47*). Genetic diversity for SARS2 is currently limited, as the virus has gone through a genetic bottleneck during the singular animal-to-human spill-over event. However, the genetic/antigenic variation will increase in time, as observed for the endemic human coronavirus HCoV-229E, which exhibits cumulative sequence variation in the RBD loops which engage its cellular receptor(48). The limited mutational space of the 47D11 epitope may confer the antibody sustainable applicability in neutralizing a wide range of future-emerging virus variants.

Methods

222 **Expression and purification of coronavirus spike proteins**

223 To express the prefusion spike ectodomain, gene encoding residues 1−1200 of SARS2 S
224 (GenBank: QHD43416.1) with proline substitutions at residues 986 and 987, a "AAARS"
225 substitution at the furin cleavage site (residues 682–685) and residues 1-1160 of SARS S
226 (GenBank: AAP13567.1) with proline substitutions at residues 956 and 957, a C-terminal T4
227 fibritin trimerization motif, a StrepTag was synthesized and cloned into the mammalian
228 expression vector pCAGGS. Similarly, pCAGGS expression vectors encoding S1 or its
229 subdomain $S1_B$ of SARS (S1, residues 1-676; $S1_B$, residues, 325-533), and SARS2 (S1,
230 residues 1-682; $S1_B$, residues 333-527) C-terminally tagged with Fc domain of human or
231 mouse IgG or Strep-tag were generated as described before(*42*). Recombinant proteins and
232 antibody 47D11 were expressed transiently in FreeStyle™ 293-F Cells (Thermo Fisher
233 Scientific) and affinity purified from the culture supernatant by protein-A sepharose beads (GE
234 Healthcare) or streptactin beads (IBA) purification. Purity and integrity of all purified
235 recombinant proteins was checked by coomassie stained SDS-PAGE.

236

237 **Pseudotyped virus neutralization assay**

238 Neutralization with SARS2-S VSV pseudotyped viruses was performed as described
239 previously (24). HEK-293T cells were transfected with pCAGGS expression vectors encoding
240 SARS2-S carrying a 18-a.a. cytoplasmic tail truncation, respectively. One day post
241 transfection, cells were infected with the VSV-G pseudotyped VSVΔG expressing the firefly
242 (*Photinus pyralis*) luciferase. Twenty-four hours later, cell supernatants containing SARS2-S
243 pseudotyped VSV particles were harvested and titrated on African green monkey kidney
244 VeroE6 (ATCC#CRL-1586) cells. In the virus neutralization assay, mAbs were threefold
245 serially diluted and mixed with an equal volume of pseudotyped VSV particles and incubated
246 for 1 hour at room temperature (RT). The virus/antibody mix was subsequently added to
247 confluent VeroE6 monolayers in 96-well plate, and incubated at 37°C. After 24 hours, cells
248 were washed and lysis buffer (Promega) was added. Luciferase activity was measured on a
249 Berthold Centro LB 960 plate luminometer using D-luciferin as a substrate (Promega). The
250 percentage of infectivity was calculated as ratio of luciferase readout in the presence of mAbs
251 normalized to luciferase readout in the absence of mAb. The half maximal inhibitory
252 concentration (IC_{50}) was determined using 4-parameter logistic regression (GraphPad Prism
253 version 8).

254

255 **ELISA analysis of antibody binding to CoV spike antigens**

256 ELISA was performed as described previously (24). Briefly, NUNC Maxisorp plates (Thermo
257 Scientific) coated with equimolar antigen amounts were blocked with 3% bovine serum
258 albumin (Bio-Connect) in PBS containing 0.1% Tween-20 at RT for 2 hours. Fourfold serial

259 dilutions of mAbs starting at 10 µg/ml (diluted in blocking buffer) were added and plates were
260 incubated for 1 hour at RT. Plates were washed three times and incubated with horseradish
261 peroxidase (HRP)-conjugated goat anti-human secondary antibody (ITK Southern Biotech)
262 diluted 1:2000 in blocking buffer for 1 hour at RT. An HRP-conjugated anti-StrepMAb (IBA)
263 antibody was used to corroborate equimolar coating of the Strep-tagged spike antigens. HRP
264 activity was measured at 450 nanometer using tetramethylbenzidine substrate (BioFX) using
265 an ELISA plate reader (EL-808, Biotek). Half-maximum effective concentration (EC_{50}) binding
266 values were calculated by non-linear regression analysis on the binding curves using
267 GraphPad Prism (version 8).
268
269 **Preparation of Fab-47D11 from IgG**
270 47D11 Fab was digested from IgG with papain using a Pierce Fab Preparation Kit (Thermo
271 Fisher Scientific), following the manufacturer's standard protocol.
272
273 **Cryo-EM sample preparation and data collection**
274 3 µL of SARS2-S or SARS-S at 1.6 mg/mL was mixed with 0.85 µL of Fab 47D11 at 4 mg/mL
275 and incubated for 50 s at RT. The sample was applied onto a freshly glow discharged R1.2/1.3
276 Quantifoil grid in a Vitrobot Mark IV (Thermo Fisher Scientific) chamber pre-equilibrated at
277 4°C and 100% humidity. The grid was immediately blotted at force 0 for 5 s and plunged into
278 liquid ethane. Data was acquired on a 200 kV Talos Arctica (Thermo Fisher Scientific)
279 equipped with a Gatan K2 Summit direct detector and Gatan Quantum energy filter operated
280 in zero-loss mode with a 20 eV slit width. To account for the preferred orientation exhibited by
281 the spike ectodomains, automated data collection at tilts 0°, 20°, and 30° was carried out using
282 EPU 2 software (Thermo Fisher Scientific), and data at tilt 40° using SerialEM(49). A nominal
283 magnification of 130,000x, corresponding to an effective pixel size of 1.08 Å, was used. Movies
284 were acquired in counting mode with a total dose of 40e/$Å^2$ distributed over 50 frames. 4,231
285 movies were acquired for SARS2 and 3,247 movies for SARS-S, with defocus ranging
286 between 0.5 µm and 3 µm.
287
288 **Cryo-EM data processing**
289 Single-particle analysis was performed in Relion version 3.1.(*50*). The data was processed in
290 four separate batches, corresponding to the stage tilt angle used for the acquisition. Drift and
291 gain correction were performed with MotionCor2(*51*), CTF parameters were estimated using
292 CTFFind4(*52*) and particles were picked using the Laplacian picker in Relion(*50*). One round
293 of 2D classification was performed on each batch of data and particles belonging to well
294 defined classes were retained. Subsequently, 3D classification was performed, using a 50 Å
295 low-pass filtered partially open conformation as an initial model (EMD-21457,(12)), without

296 imposing symmetry. All particles belonging to Fab bound class were then selected for 3D auto-
297 refinement. Before merging the different batches, iterative rounds of per particle CTF
298 refinement, 3D auto-refinement and post-processing were used to account for the stage tilt
299 used during data collection. The refined particle star files from each batch were then combined
300 and subjected to a final round of 3D auto refinement, per particle defocus estimation, 3D auto-
301 refinement and post processing, both with and without imposed C3 symmetry. Overviews of
302 the single-particle image processing pipelines are shown in supplementary figure 6 and 7.
303
304 **Model building and refinement**
305 UCSF Chimera (version 1.12.0) and Coot (version, 1.0.) were used for model building and
306 analysis(*53*, *54*). The SARS2-S model, in the partially open conformation (one RBD up, pdb
307 6VYB)(*12*), was used for the spike and fitted into our density using the UCSF Chimera 'Fit in
308 map' tool(*53*). For SARS a closed protomer of the pdb 6NB6 was used as starting model(*55*).
309 To build a model for the Fab the sequence of the variable regions of the HC and the LC were
310 separately blasted against the pdb. For the HC variable region, the corresponding region of
311 the pdb 6IEB (human monoclonal antibody R15 against RVFV Gn) was used(*56*). The LC
312 variable region was modelled using the pdb 6FG1 as template (Fab Natalizumab)(*57*). For
313 both chains, the query sequence of 47D11 was aligned to the template sequence. Sequence
314 identity was particularly high (87% and 97% for the HC and LC, respectively). Phenix sculptor
315 was used to create an initial model for the Fab chains(*58*), removing the non-aligning regions
316 (notably the CDRH3). This model was fitted into our density and the missing regions were built
317 manually in the density map using Coot(*54*). Models were refined against the respective EM
318 density maps using Phenix Real Space Refinement and Isolde(*59*)(*60*), and validated with
319 MolProbity and Privateer (glycans)(*59*, *61-63*).
320
321 **Analysis and visualisation**
322 PDBePISA was used to identify spike residues interacting with 47D11(*64*). Surface colouring
323 of the SARS-CoV-2 RBD using the Kyte-Doolittle hydrophobicity scale was performed in
324 UCSF chimera(*53*). Volume measurements were performed using CASTp 3.0, using a probe
325 radius of 1.2 Å(*65*). In order to colour the 47D11 bound RBD surface according to each
326 residues mean mutational effect on expression, the pdb file was populated with the mean
327 mutation effect on expression values described by Starr et al(*45*). The UCSF Chimera
328 'MatchMaker' tool was used to obtain RMSD values, using default settings. Figures were
329 generated using UCSF Chimera(*53*) and UCSF ChimeraX(*66*).
330
331 **Figure Legends**

Figure 1: **47D11 has differing conformational selectivity for the SARS-CoV and SARS-CoV-2 spike.** A) Surface rendering of the fully closed SARS spike bound to three 47D11 antibody Fab fragments, shown as two orthogonal views. (B) Surface rendering of the partially open SARS2 spike in complex with two 47D11 antibody Fab fragments, shown as two orthogonal views. The spike protomers are coloured pink, blue and grey, and the 47D11 heavy and light chain are coloured yellow and purple, respectively. For clarity, only the Fab variable region is shown.

Figure 2: **47D11 binds specifically to the closed RBD and prevents their full compaction.** A) Top view of the 47D11 bound SARS2 spike. The spike protomers are coloured pink, blue and grey, and the 47D11 heavy and light chain are coloured yellow and purple, respectively. Glycans, and the N-terminal domain, are omitted for clarity and only the Fab variable region is shown. The superposed structure of the partially open apo SARS2 spike (PDB ID: 6ZGG) is shown as a silhouette. B) Zoomed in view of the boxed region in panel A. C) Zoomed in view of the SARS2 open RBD and adjacent NTD. The overlaid 47D11 Fab is shown semi-transparent and the N343 glycan is shown in ball-and-stick representation and coloured tan. D) Top view of the 47D11 bound SARS2 spike coloured as shown in panel A. The superposed structure of the closed apo SARS spike (PDB ID: 5XLR) is shown as a silhouette. E) Zoomed in view of the boxed region in panel D, showing a putative salt bridge between the 47D11 variable light chain and the RBD loop. F) ELISA-binding curves of 47D11 binding to wildtype and loop swapped spike ectodomains.

Figure 3: **The 47D11 epitope comprises a mutationally constrained hydrophobic pocket which is normally shielded by glycan N343.** A) Ribbon diagram of the SARS2-S receptor-binding domain (RBD) in complex with the 47D11 antibody Fab fragment. For comparison, residues 1-84 of the RBD bound ACE2 (PDB ID: 6M0J) are shown as a silhouette. B) Close-up view of the 47D11 epitope with the hydrophobic pocket residues shown as sticks and coloured dark blue. The N343 glycan is shown in ball-and-stick representation and coloured tan. For clarity, only the core pentasaccharide is shown. C) Slice through the surface rendered 47D11 bound SARS2-S RBD. D) Equivalent view as shown in panel C for the apo RBD (PDB ID:6VYB). E) Relative surface binding of 47D11, (F) ACE2, (G) CR3022 and (H) an anti-FLAG antibody to full-length SARS2 spike epitope mutants, determined by fluorescence-activated cell sorting. I) Antibody-mediated neutralization of infection of luciferase-encoding VSV particles pseudotyped with wild-type, V367A or V367F SARS2-S. J) Surface representation of the 47D11 bound SARS2-S RBD coloured according to mean mutation effect on expression (red indicates more constrained)(*45*). The Fab is shown as a ribbon diagram. K) As shown in E for the S309 bound SARS2 RBD.

369 **Figure 4: The 47D11 epitope is conserved in SARS-like viruses.** A) Surface representation
370 of the 47D11 bound RBD coloured according to sequence conservation across SARS-1,
371 SARS2 and 11 SARS-like viruses (Supplementary Figure 5). The 47D11 Fab variable chains
372 are shown as a ribbon diagram and coloured grey. Heavy chain residues W102 and F103 are
373 shown as sticks. For comparison, residues 1-84 of the RBD bound ACE2 (PDB ID: 6M0J) are
374 shown as a silhouette. B) ELISA-binding curves of 47D11 to the S1B domain of SARS,
375 SARS2, WIV16, HKU3-3 and HKU9-3. The average ± SD from two independent experiments
376 with technical duplicates is shown. C) Aligned RBD sequences of SARS2, SARS-1, WIV16,
377 HKU3-3 and HKU9-3. Key residues in the 47D11 epitope are indicated by red arrows.
378
379

380 **Figure 1**

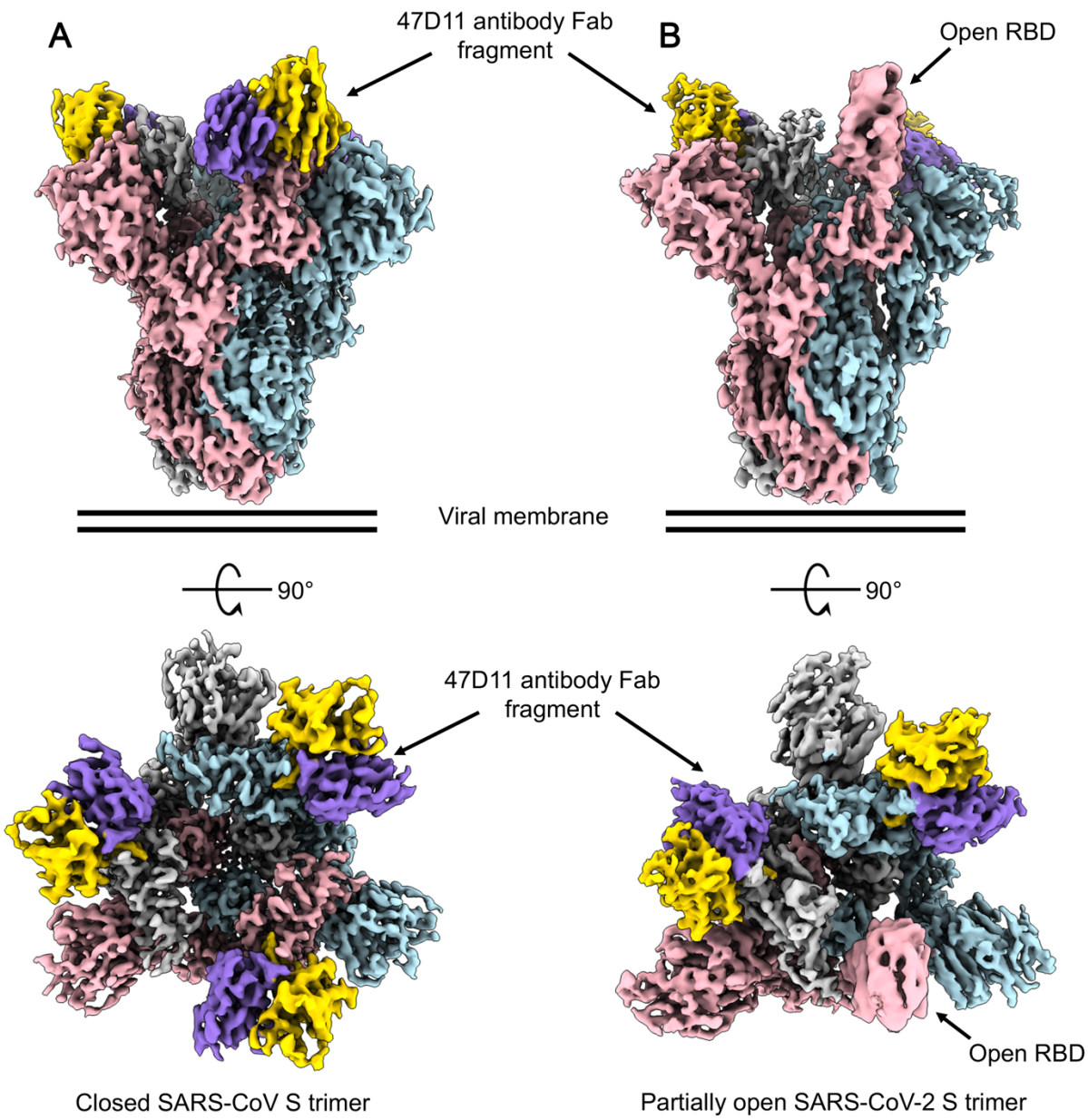

381

382

383 **Figure 2**

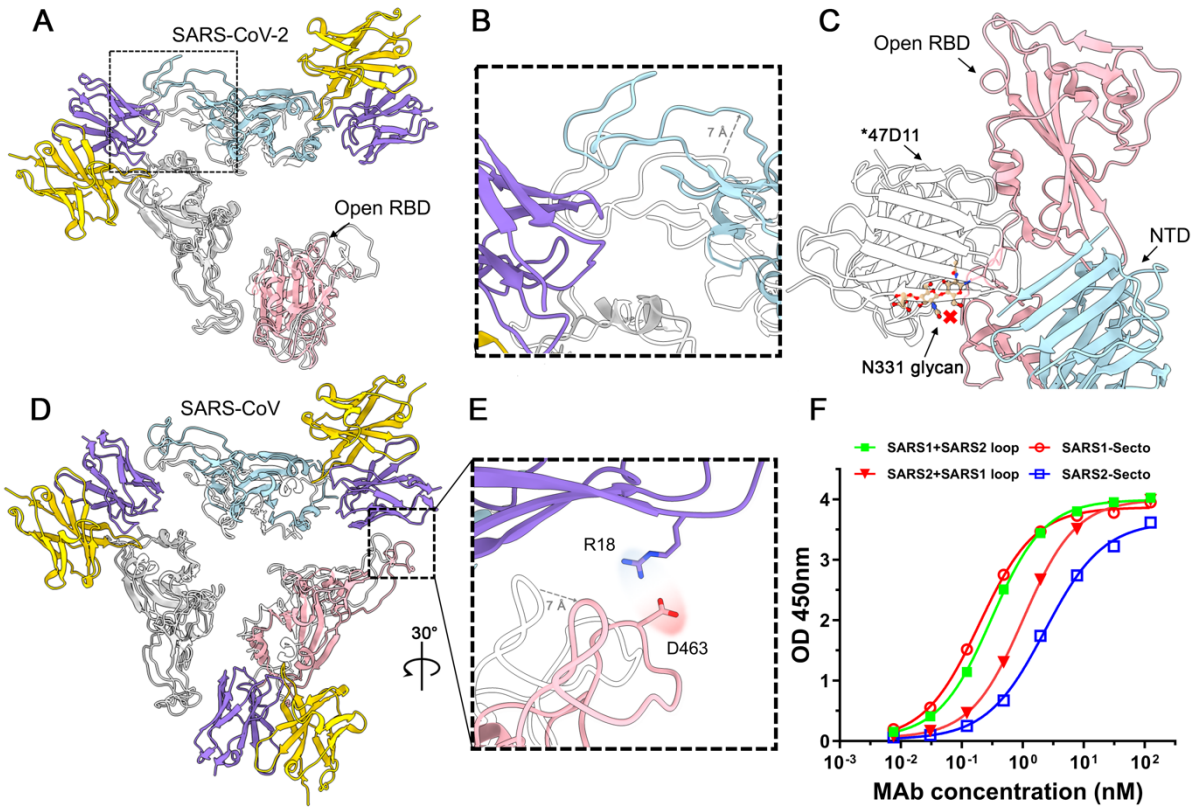

384

Figure 3

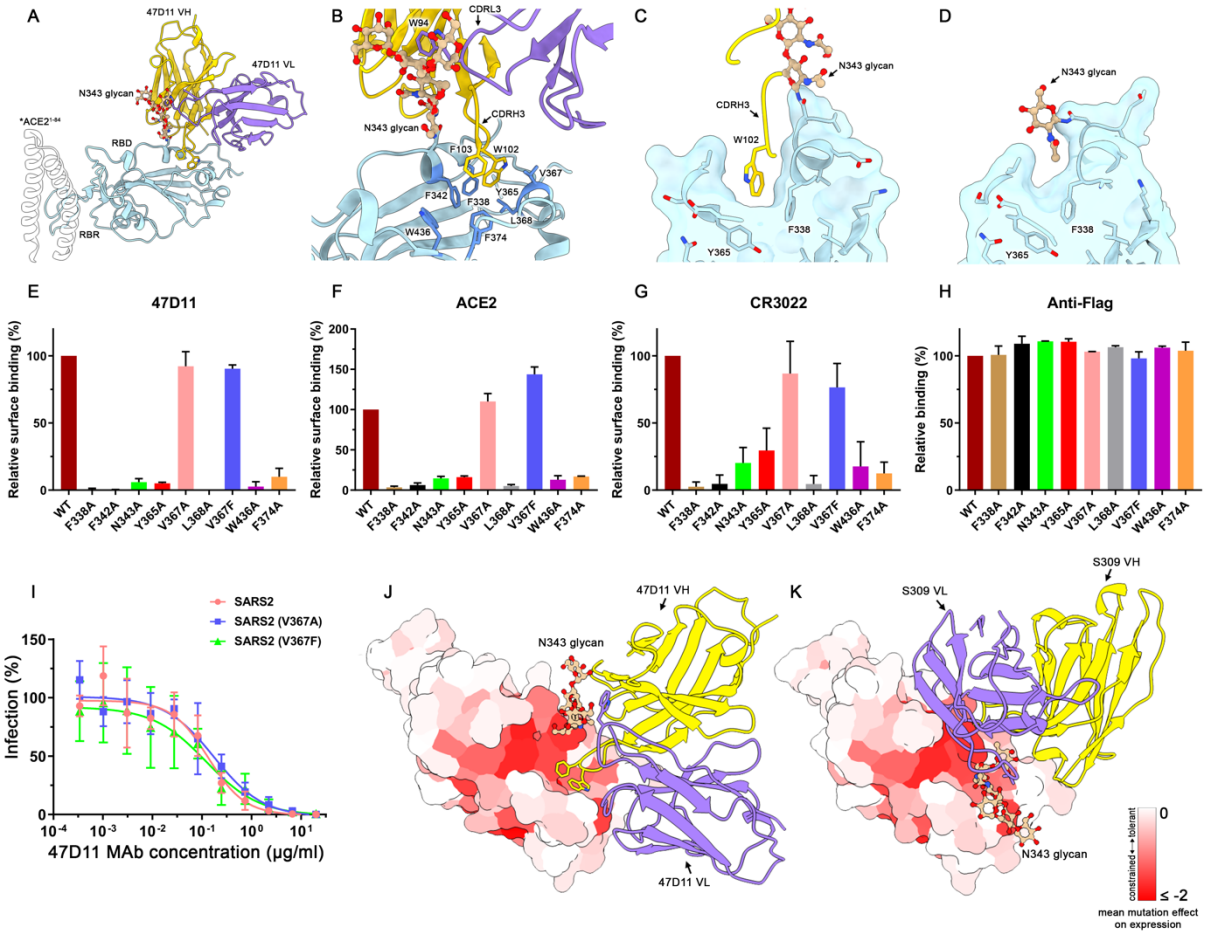
A
47D11 VH
47D11 VL
N343 glycan
*ACE2
RBD
RBR
B
W94
CDRL3
CDRH3
N343 glycan
F103
W102
V367
F342
F338
Y365
L368
W436
F374
C
N343 glycan
CDRH3
W102
F338
Y365
D
N343 glycan
F338
Y365
E
47D11
Relative surface binding (%)
F
ACE2
Relative surface binding (%)
G
CR3022
Relative surface binding (%)
H
Anti-Flag
Relative binding (%)
WT
F338A
F342A
N343A
Y365A
V367A
L368A
V367F
W436A
F374A
I
SARS2
SARS2 (V367A)
SARS2 (V367F)
Infection (%)
47D11 MAb concentration (μg/ml)
J
47D11 VH
N343 glycan
47D11 VL
K
S309 VH
S309 VL
N343 glycan
constrained ← → tolerant
0
≤ -2
mean mutation effect on expression

Figure 4

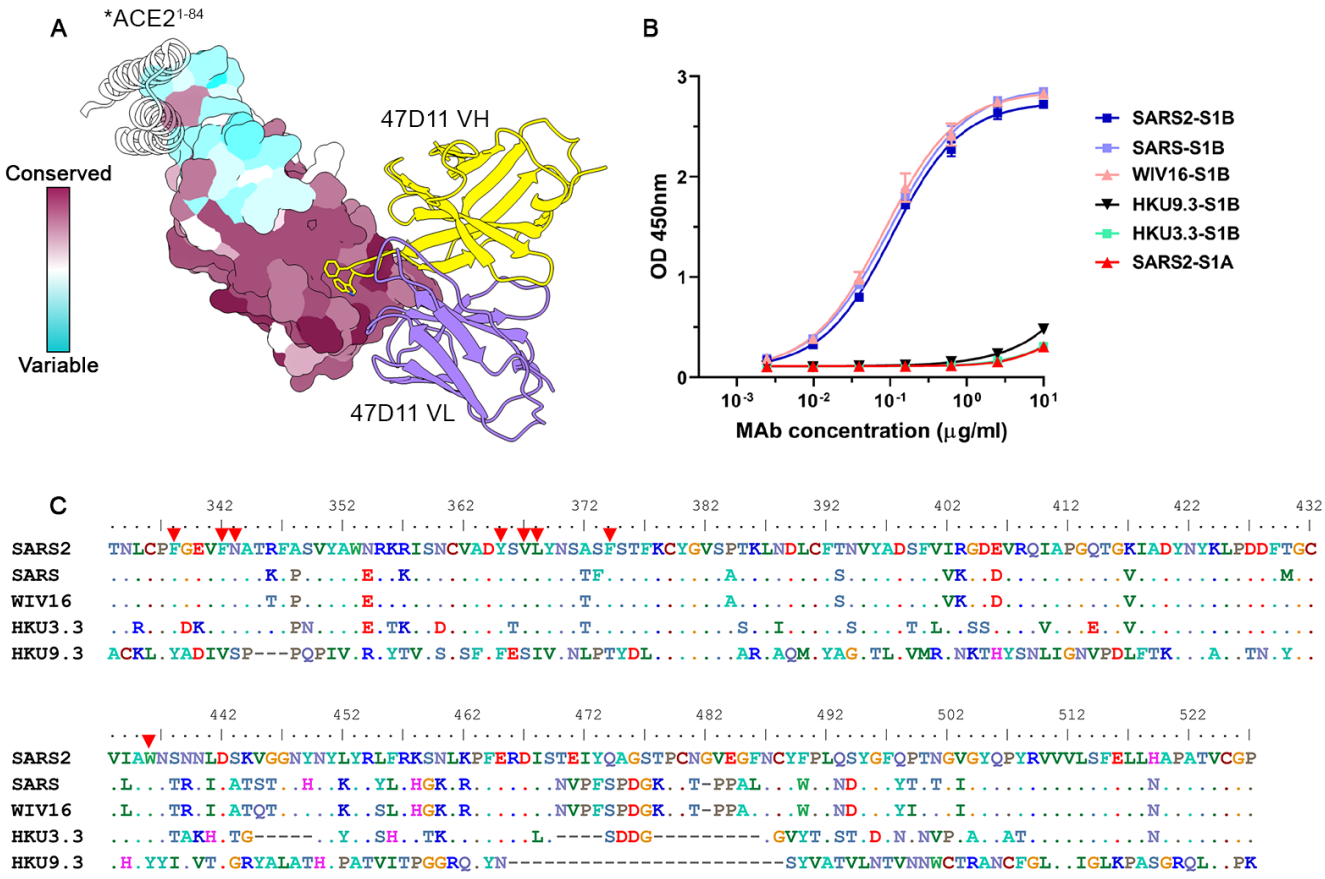

Data availability

Coordinates for the 47D11-bound SARS-CoV and SARS-CoV-2 spike proteins are deposited in the Protein Data Bank under accession codes XXXX and XXXX, respectively. The corresponding EM density maps have been deposited to the Electron Microscopy Data Bank under the accessions EMD-XXXX and EMD-XXXX. All reagents and relevant data are available from the authors upon request.

Acknowledgements

This work was supported by the European Research Council under the European Union's Horizon2020 Programme (ERC Consolidator Grant Agreement 724425 - BENDER). J.F. and D.L.H. are funded from the European Union's Horizon 2020 research and innovation program under the Marie Skłodowska-Curie grant agreement (No 792575 and 842333). J.F. and D.L.H. also hold EMBO non-stipendiary long-term Fellowships (ALTF 948-2017 and ALTF 1172-2018). Research reported in this publication was supported by a China Scholarship Council grant to C.W. (CSC201708620178). We thank Dr Mihajlo Vanevic for IT support.

404 **Author contributions**

405 J.F., D.L.H., C.W., W.L., F.J.M.K., F.F. and B.J.B. conceived, designed, and coordinated the
406 study. J.F., D.L.H., C.W., W.L., I.D., G.O., and S.H. conducted the experiments. F.J.M.K, F.F.
407 and B.J.B. supervised part of the experiments. All authors contributed to the interpretations
408 and conclusions presented. J.F. D.L.H. and B.J.B. wrote the manuscript, J.F., D.L.H, C.W.,
409 W.L. F.F. and B.J.B participated in editing the manuscript.

410 **Competing interests**

411 A patent application has been filed on 12 March 2020 on monoclonal antibodies targeting
412 SARS-CoV-2 (United Kingdom patent application no. 2003632.3; patent applicants: Utrecht
413 University, Erasmus Medical Center and Harbour BioMed). I.D. is an employee of Thermo
414 Fisher Scientific. The other authors declare no competing interests.

415

416 **Corresponding authors**

417 Correspondence to Friedrich Förster (f.g.forster@uu.nl) and Berend-Jan Bosch
418 (b.j.bosch@uu.nl).

419

420 **References**

421 1. P. Zhou *et al.*, A pneumonia outbreak associated with a new coronavirus of probable
422 bat origin. *Nature*. **579**, 270–273 (2020).

423 2. T. G. Ksiazek *et al.*, A novel coronavirus associated with severe acute respiratory
424 syndrome. *N. Engl. J. Med.* **348**, 1953–1966 (2003).

425 3. Coronaviridae Study Group of the International Committee on Taxonomy of Viruses,
426 (Nature Publishing Group, 2020), vol. 5, pp. 536–544.

427 4. P. Prabakaran *et al.*, Potent human monoclonal antibodies against SARS CoV, Nipah
428 and Hendra viruses. *Expert Opin Biol Ther*. **9**, 355–368 (2009).

429 5. E. O. Saphire, S. L. Schendel, B. M. Gunn, J. C. Milligan, G. Alter, Antibody-mediated
430 protection against Ebola virus. *Nat. Immunol.* **19**, 1169–1178 (2018).

431 6. A. Casadevall, L.-A. Pirofski, The convalescent sera option for containing COVID-19.
432 *J. Clin. Invest.* **130**, 1545–1548 (2020).

433 7. A. C. Cunningham, H. P. Goh, D. Koh, Treatment of COVID-19: old tricks for new
434 challenges. *Crit Care*. **24**, 91–2 (2020).

435 8. F. Li, Structure, Function, and Evolution of Coronavirus Spike Proteins.
436 *http://dx.doi.org/10.1146/annurev-virology-110615-042301*. **3**, 237–261 (2016).

437 9. B.-J. Bosch, R. van der Zee, C. A. M. de Haan, P. J. M. Rottier, The coronavirus spike
438 protein is a class I virus fusion protein: structural and functional characterization of the
439 fusion core complex. *Journal of Virology*. **77**, 8801–8811 (2003).

440 10. M. Gui *et al.*, Cryo-electron microscopy structures of the SARS-CoV spike glycoprotein
441 reveal a prerequisite conformational state for receptor binding. *Cell Res.* **27**, 119–129
442 (2017).

443 11. D. Wrapp *et al.*, Cryo-EM structure of the 2019-nCoV spike in the prefusion
444 conformation. *Science*. **367**, 1260–1263 (2020).

445 12. A. C. Walls *et al.*, Structure, Function, and Antigenicity of the SARS-CoV-2 Spike
446 Glycoprotein. *Cell*. **181**, 281–292.e6 (2020).

447 13. J. Lan *et al.*, Structure of the SARS-CoV-2 spike receptor-binding domain bound to the
448 ACE2 receptor. *Nature*. **579**, 1–6 (2020).

449 14. R. Yan *et al.*, Structural basis for the recognition of SARS-CoV-2 by full-length human
450 ACE2. *Science*. **367**, 1444–1448 (2020).

451 15. M. Hoffmann *et al.*, SARS-CoV-2 Cell Entry Depends on ACE2 and TMPRSS2 and Is
452 Blocked by a Clinically Proven Protease Inhibitor. *Cell*. **181**, 271–280.e8 (2020).

453 16. A. C. Walls *et al.*, Tectonic conformational changes of a coronavirus spike glycoprotein
454 promote membrane fusion. *Proc. Natl. Acad. Sci. U.S.A.* **114**, 11157–11162 (2017).

455 17. Y. Cai *et al.*, Distinct conformational states of SARS-CoV-2 spike protein. *Science*,
456 eabd4251 (2020).

457 18. D. van Riel, E. de Wit, Next-generation vaccine platforms for COVID-19. *Nat. Mater.*
458 **19**, 810–812 (2020).

459 19. J. Hansen *et al.*, Studies in humanized mice and convalescent humans yield a SARS-
460 CoV-2 antibody cocktail. *Science*. **369**, 1010–1014 (2020).

461 20. P. J. M. Brouwer *et al.*, Potent neutralizing antibodies from COVID-19 patients define
462 multiple targets of vulnerability. *Science*. **369**, 643–650 (2020).

463 21. R. Shi *et al.*, A human neutralizing antibody targets the receptor-binding site of SARS-
464 CoV-2. *Nature*. **584**, 120–124 (2020).

465 22. S. J. Zost *et al.*, Potently neutralizing and protective human antibodies against SARS-
466 CoV-2. *Nature*. **584**, 443–449 (2020).

467 23. S. J. Zost *et al.*, Rapid isolation and profiling of a diverse panel of human monoclonal
468 antibodies targeting the SARS-CoV-2 spike protein. *Nat. Med.* **26**, 1422–1427 (2020).

469 24. D. F. Robbiani *et al.*, Convergent antibody responses to SARS-CoV-2 in convalescent
470 individuals. *Nature*. **584**, 437–442 (2020).

471 25. T. F. Rogers *et al.*, Isolation of potent SARS-CoV-2 neutralizing antibodies and
472 protection from disease in a small animal model. *Science*. **369**, 956–963 (2020).

473 26. Y. Cao *et al.*, Potent neutralizing antibodies against SARS-CoV-2 identified by high-
474 throughput single-cell sequencing of convalescent patients' B cells. *Cell* (2020),
475 doi:10.1016/j.cell.2020.05.025.

476 27. M. Yuan *et al.*, A highly conserved cryptic epitope in the receptor binding domains of
477 SARS-CoV-2 and SARS-CoV. *Science*. **368**, 630–633 (2020).

478 28. W. Li *et al.*, Potent neutralization of SARS-CoV-2 in vitro and in an animal model by a
479 human monoclonal antibody. *bioRxiv*. **525**, 129 (2020).

480 29. A. Z. Wec *et al.*, Broad neutralization of SARS-related viruses by human monoclonal
481 antibodies. *Science*. **369**, 731–736 (2020).

482 30. B. Ju *et al.*, Human neutralizing antibodies elicited by SARS-CoV-2 infection. *Nature*.
483 **584**, 115–119 (2020).

484 31. Y. Wu *et al.*, A noncompeting pair of human neutralizing antibodies block COVID-19
485 virus binding to its receptor ACE2. *Science*. **368**, 1274–1278 (2020).

486 32. E. Seydoux *et al.*, Analysis of a SARS-CoV-2-Infected Individual Reveals Development
487 of Potent Neutralizing Antibodies with Limited Somatic Mutation. *Immunity*. **53**, 98–
488 105.e5 (2020).

489 33. C. O. Barnes *et al.*, Structures of Human Antibodies Bound to SARS-CoV-2 Spike
490 Reveal Common Epitopes and Recurrent Features of Antibodies. *Cell*. **182**, 828–
491 842.e16 (2020).

492 34. H. Lv *et al.*, Cross-reactive Antibody Response between SARS-CoV-2 and SARS-CoV
493 Infections. *Cell Rep*. **31**, 107725 (2020).

494 35. D. Pinto *et al.*, Cross-neutralization of SARS-CoV-2 by a human monoclonal SARS-
495 CoV antibody. *Nature*. **583**, 1–10 (2020).

496 36. D. Zhou *et al.*, Structural basis for the neutralization of SARS-CoV-2 by an antibody
497 from a convalescent patient. *Nat. Struct. Mol. Biol.* **20**, 773–9 (2020).

498 37. H. Liu *et al.*, Cross-neutralization of a SARS-CoV-2 antibody to a functionally conserved
499 site is mediated by avidity. *bioRxiv* (2020), doi:10.1101/2020.08.02.233536.

500 38. Z. Lv *et al.*, Structural basis for neutralization of SARS-CoV-2 and SARS-CoV by a
501 potent therapeutic antibody. *Science*. **369**, 1505–1509 (2020).

502 39. X. Chi *et al.*, A neutralizing human antibody binds to the N-terminal domain of the Spike
503 protein of SARS-CoV-2. *Science*. **369**, 650–655 (2020).

504 40. B. R. West *et al.*, Structural Basis of Pan-Ebolavirus Neutralization by a Human
505 Antibody against a Conserved, yet Cryptic Epitope. *MBio*. **9**, 365 (2018).

506 41. Y. Yuan *et al.*, Cryo-EM structures of MERS-CoV and SARS-CoV spike glycoproteins
507 reveal the dynamic receptor binding domains. *Nat Commun*. **8**, 15092–9 (2017).

508 42. C. Wang *et al.*, A human monoclonal antibody blocking SARS-CoV-2 infection. *Nat*
509 *Commun*. **11**, 2251–6 (2020).

510 43. C. Toelzer *et al.*, Free fatty acid binding pocket in the locked structure of SARS-CoV-2
511 spike protein. *Science*, eabd3255 (2020).

512 44. T. Koyama, D. Platt, L. Parida, Variant analysis of SARS-CoV-2 genomes. *Bull. World*
513 *Health Organ.* **98**, 495–504 (2020).

514 45. T. N. Starr *et al.*, Deep Mutational Scanning of SARS-CoV-2 Receptor Binding Domain
515 Reveals Constraints on Folding and ACE2 Binding. *Cell* (2020),
516 doi:10.1016/j.cell.2020.08.012.

517 46. D. Wrapp *et al.*, Structural Basis for Potent Neutralization of Betacoronaviruses by
518 Single-Domain Camelid Antibodies. *Cell*. **181**, 1004–1015.e15 (2020).

519 47. M. A. Tortorici *et al.*, Ultrapotent human antibodies protect against SARS-CoV-2
520 challenge via multiple mechanisms. *Science*. **4**, eabe3354 (2020).

521 48. A. H. M. Wong *et al.*, Receptor-binding loops in alphacoronavirus adaptation and
522 evolution. *Nat Commun*. **8**, 1735–10 (2017).

523 49. M. Schorb, I. Haberbosch, W. J. H. Hagen, Y. Schwab, D. N. Mastronarde, Software
524 tools for automated transmission electron microscopy. *Nat. Methods*. **16**, 471–477
525 (2019).

526 50. J. Zivanov, T. Nakane, S. H. W. Scheres, A Bayesian approach to beam-induced
527 motion correction in cryo-EM single-particle analysis. *IUCrJ*. **6**, 5–17 (2019).

528 51. S. Q. Zheng *et al.*, MotionCor2: anisotropic correction of beam-induced motion for
529 improved cryo-electron microscopy. *Nat. Methods*. **14**, 331–332 (2017).

530 52. A. Rohou, N. Grigorieff, CTFFIND4: Fast and accurate defocus estimation from electron
531 micrographs. *Journal of Structural Biology*. **192**, 216–221 (2015).

532 53. E. F. Pettersen *et al.*, UCSF Chimera--a visualization system for exploratory research
533 and analysis. *J Comput Chem*. **25**, 1605–1612 (2004).

534 54. P. Emsley, K. Cowtan, Coot: model-building tools for molecular graphics. *Acta*
535 *Crystallogr. D Biol. Crystallogr.* **60**, 2126–2132 (2004).

536 55. A. C. Walls *et al.*, Unexpected Receptor Functional Mimicry Elucidates Activation of
537 Coronavirus Fusion. *Cell*. **176**, 1026–1039.e15 (2019).

538 56. Q. Wang *et al.*, Neutralization mechanism of human monoclonal antibodies against Rift
539 Valley fever virus. *Nat Microbiol*. **4**, 1231–1241 (2019).

540 57. A. Cassotta *et al.*, A single T cell epitope drives the neutralizing anti-drug antibody
541 response to natalizumab in multiple sclerosis patients. *Nat. Med.* **25**, 1402–1407
542 (2019).

543 58. G. Bunkóczi, R. J. Read, Improvement of molecular-replacement models with Sculptor.
544 *Acta Crystallogr. D Biol. Crystallogr.* **67**, 303–312 (2011).

545 59. J. J. Headd *et al.*, Use of knowledge-based restraints in phenix.refineto improve
546 macromolecular refinement at low resolution. *Acta Crystallogr. D Biol. Crystallogr.* **68**,
547 381–390 (2012).

548 60. T. I. Croll, ISOLDE: a physically realistic environment for model building into low-
549 resolution electron-density maps. *Acta Crystallogr D Struct Biol*. **74**, 519–530 (2018).

550 61. V. B. Chen *et al.*, MolProbity: all-atom structure validation for macromolecular
551 crystallography. *Acta Crystallogr. D Biol. Crystallogr.* **66**, 12–21 (2010).

552 62. J. Agirre *et al.*, Privateer: software for the conformational validation of carbohydrate
553 structures. *Nat. Struct. Mol. Biol.* **22**, 833–834 (2015).

554 63. J. Agirre, G. Davies, K. Wilson, K. Cowtan, Carbohydrate anomalies in the PDB. *Nat.*
555 *Chem. Biol.* **11**, 303–303 (2015).

556 64. E. Krissinel, K. Henrick, Inference of macromolecular assemblies from crystalline state.
557 *J. Mol. Biol.* **372**, 774–797 (2007).

558 65. W. Tian, C. Chen, X. Lei, J. Zhao, J. Liang, CASTp 3.0: computed atlas of surface
559 topography of proteins. *Nucleic Acids Res.* **46**, W363–W367 (2018).

560 66. T. D. Goddard *et al.*, UCSF ChimeraX: Meeting modern challenges in visualization and
561 analysis. *Protein Sci.* **27**, 14–25 (2018).

562